TURBO-16-1281

# ENDWALL LOSS IN TURBINE CASCADES

**John D. Coull**
Whittle Laboratory, University of Cambridge, UK
jdc38@cam.ac.uk

## ABSTRACT

Prior to the detailed design of components, turbomachinery engineers must guide a mean-line or throughflow design towards an optimum configuration. This process requires a combination of informed judgement and low-order correlations for the principle sources of loss. With these requirements in mind, this paper examines the impact of key design parameters on endwall loss in turbines, a problem which remains poorly understood.

The paper presents a parametric study of linear cascades, which represent a simplified model of real-engine flow. The designs are nominally representative of the Low Pressure Turbine blades of an aero engine, with varying flow angles, blade thickness and suction surface lift styles. RANS calculations are performed for a single aspect ratio and constant inlet boundary layer thickness.

The paper first examines the two-dimensional design space before studying endwall losses in detail. It is demonstrated that endwall loss can be decomposed into two components: one due to the dissipation associated with the endwall boundary layer; and another induced by the secondary flows. This secondary-flow-induced loss is found to scale with a measure of streamwise vorticity predicted by classical secondary flow theory.

## 1 INTRODUCTION

Endwall effects generate around a third of the total aerodynamic loss in a turbine [1]. These losses are generated by dissipation in the hub and casing boundary layers and by the secondary flow, which is generated as the non-uniform inlet flow turns through the blade row.

Much of the fundamental understanding of endwall flows has been built on studies of linear cascades, which represent an approximate model for real-engine behavior. Early theoretical work focused on predicting the secondary flows in an inviscid flowfield by considering the convection of vortex filaments through a cascade (e.g. [2]). More detailed understanding of the flow behavior was gleaned over many decades of experimental research, as summarized by Sieverding [3] and Langston [4].

Figure 1 shows a diagram based on one of the current RANS simulations, where vortex structures have been visualized using the eigenvalue method of Adrian et al. [5]. The endwall is subject to the same static pressure field as the freestream flow; the incoming endwall boundary layer therefore separates in the adverse pressure gradient approaching the blade leading edge, and rolls up into a horseshoe vortex (HSV). Once formed, the trajectory of this vortex largely follows the static pressure gradients: the suction-side leg

(HSV-SS) initially remains close to the blade suction surface corner, while the pressure side leg (HSV-PS) is driven across the passage towards the low pressure region on the adjacent blade suction surface. This leg entrains fluid from the fresh endwall boundary layer downstream of the HSV separation, and forms into the main Passage Vortex.

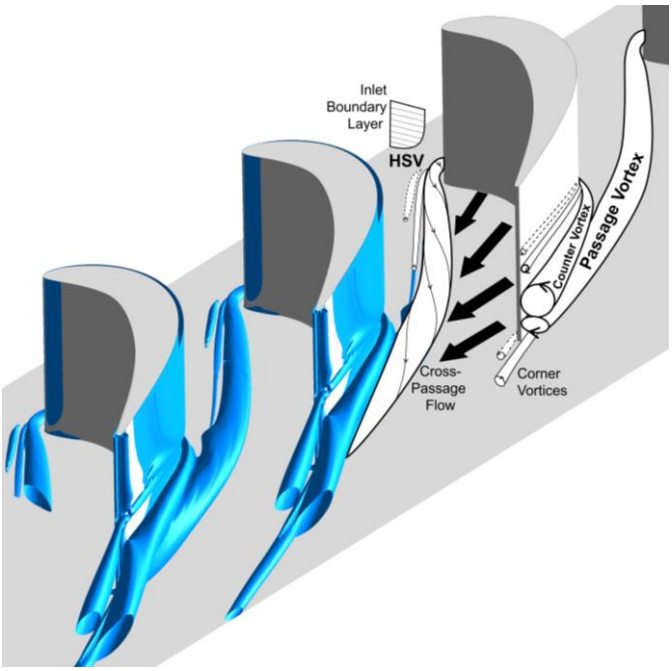


*Figure 1: Secondary Flow in a Turbine Cascade.*

On reaching the blade suction surface, the Passage Vortex interacts with the HSV-SS (Counter Vortex) from the adjacent horseshoe vortex and the blade surface, inducing large velocity gradients and high dissipation rates in this region [6]. The two vortices then move up the blade suction surface towards midspan. Other, smaller vortical structures are also observed: additional vortices are induced on the blade suction surface by the interaction of the passage and counter vortices; the HSV is actually a *system* of counter-rotating vortices, as is evident in Figure 1; and corner vortices are often generated where the cross-flow separates at the blade-endwall junctions. Downstream of the trailing edge the vortex system interacts with the trailing shed vorticity, which arises due to the variation in loading along the blade span (e.g. [7]). Deviations to this basic flow pattern have been reported by various authors, particularly in regards to the interaction of the two main vortex legs and the smaller flow features, suggesting that the detailed behavior is design-dependent. Furthermore, this description of the mean flow field neglects any unsteady effects that will be present.

At the preliminary design stage the losses introduced by the endwall flow must be modeled, prior to detailed design of the blade shape. This process must therefore rely on low-order loss correlations. Several such methods are available in the open literature, for example Ainley and Mathieson [8], Dunham and Came [9], Kacker and Okapuu [10], Craig and Cox [11] and Traupel [12]. Many of these correlations remain in use today, but they are based on the circular-arc blading typical of pre-1970 designs and some have little

physical basis. More recently, Benner et al. [13] formulated a correlation based on a survey of experimental cascade data. However, the dataset was relatively sparse and did not exhibit clear trends; furthermore there were several inconsistences in the measurement and processing techniques for each cascade. Thus it was not clear which design parameters needed to be included, or what form the correlation should take. Coull and Hodson [14] showed that the available correlations vary widely in their predictions and their sensitivity to key design parameters.

With no consistent trends available from modeling or published data, the low-order design sensitivities for turbine endwall loss remain poorly understood. The author believes that the best way to address this problem is through the study of parametric designs. A turbine cascade has at least 13 *key* independent design and operating parameters (see Table 1), which set the flow angles, aspect ratio, operating condition, suction surface pressure distribution and blade thickness. Exploring this multi-dimensional design space experimentally, or with high-order techniques such as Large Eddy Simulation, would be a huge undertaking and is unlikely to be viable. Instead this paper uses an automated RANS approach to study a large number of designs. Nonetheless it is infeasible to cover all of the design parameters in a single paper. A single aspect ratio is studied, as it is known that endwall loss is inversely proportionality to aspect ratio for sufficiently large values (e.g. [15]). A turbulent collinear boundary layer of fixed height is set at the inlet for all cases; therefore this paper does not consider the impact of inlet conditions, which can impact the endwall flow in cascades and engines (e.g. [6]).

The following section details the design and CFD methods employed. The subsequent sections focus on the impact of flow angles, examining the two-dimensional design space (section 3) and profile losses (section 4). Endwall loss is then discussed in section 5 for a larger range of designs.

## 2 NUMERICAL METHODS

### 2.1 Parametric Blade Design

An iterative two-dimensional blade design code has been developed which performs simulations using the coupled Euler and boundary layer integral solver, Mises ([16], [17]). The code is designed to carefully control the freestream velocity distribution over the suction surface boundary layer, which is key to controlling the profile loss (e.g. [18]). The code adjusts the blade shape and pitch to achieve the desired suction surface aerodynamics and exit flow conditions. The thickness distribution of the blade is also specified. To ensure the designs are tolerant to incidence, additional Mises calculations with 10° of positive incidence are executed. Leading edge over-speed spikes are minimized by using a continuous curvature geometry ([19]) and by iteratively drooping the blade leading edge.

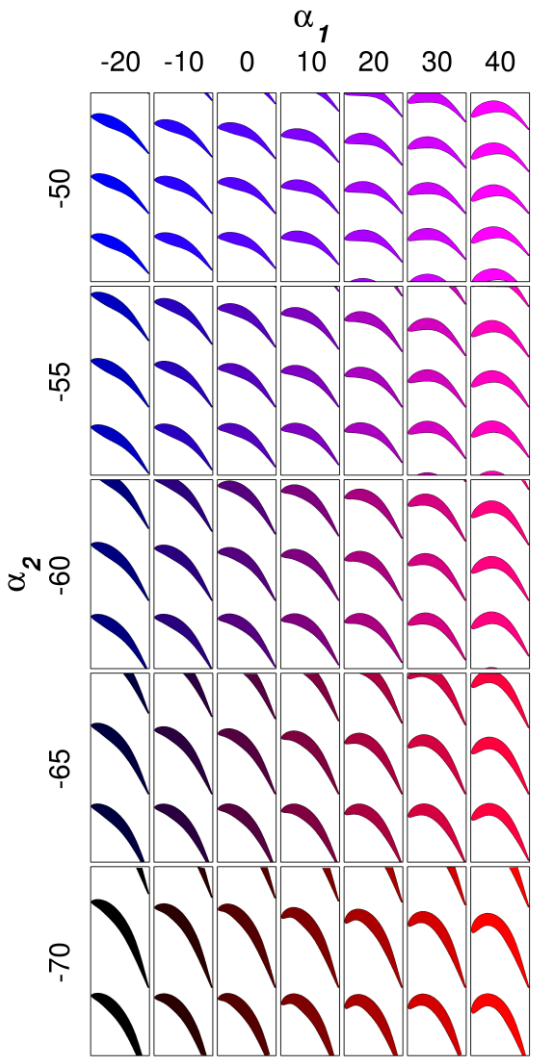


*Figure 2: Designs with varying flow angles, see Table 1.*

Figure 2 shows a set of thirty-five blades produced by varying inlet and exit flow angles while keeping all other input parameters constant. The key design parameters for this set are shown in Table 1. The suction surface aerodynamic parameters ($DF$=0.28, $PSL$=0.52) correspond to Design D studied by Coull et al. [18], which is nominally representative of modern low pressure turbine designs. The surface pressure coefficient ($C_p$) distributions predicted by Mises are shown in Figure 3(a); boundary layer transition on the suction surface has been specified at the peak velocity location (52%). It is clear from this graph that the trailing edge pressure varies significantly around the design space, a factor that has previously been observed by other authors (e.g. [20]). Normalizing $C_p$ by the trailing edge value, Figure 3(b) demonstrates that the suction surface $C_{p-TE}$ distribution is approximately constant for all of the designs. Some differences are noted in the leading edge region of the suction surface for the three designs in the top-right corner of Figure 2. These designs have the lowest pitch and therefore the blade thickness introduces significant blockage, increasing the velocity in the early

portion of the passage above the aerodynamic targets. Significant variation in pressure surface loading is observed in Figure 3 and will be discussed in section 3.2 below.

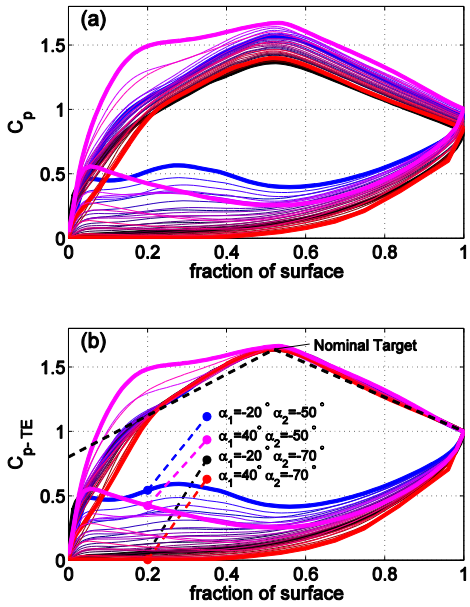


*Figure 3: Mises $C_p$ distributions for the designs in Figure 2.*

*Table 1: Key Design Parameters for the blades in Figure 2, with approximate tolerances used in the Mises design code.*

| | | Target | Tolerance |
|---|---|---|---|
| Inlet Flow Angle $\alpha_1$ | | -20°→ 40° | - |
| Outlet Flow Angle $\alpha_2$ | | -50°→ -70° | ±0.02° |
| Midspan Exit Mach number $M_2$ | | 0.7 | ±0.005 |
| Reynolds number $Re_{C_x}$ | | 200,000 | ±1% |
| Aspect Ratio $h/C_x$ | | 3 | - |
| Inlet momentum thickness $\theta/C_x$ | | 0.01 | - |
| Suction Side $C_p$ | Diffusion Factor $DF$ | 0.28 | ±0.001 |
| | Peak Suction Location $PSL$ | 0.52 | ±0.005 |
| | Leading Edge Ratio $\sqrt{C_{P-LE}/C_{p-peak}}$ | 0.7* | - |
| Thickness | Max. Thick. $T_{max}/C_x$ | 0.20 | ±0.02 |
| | Max. Thick. Location $(x/C_x)$ | 0.35 | ±0.04 |
| | TE Thickness $t/C_x$ | 0.02 | 0 |
| | TE wedge angle | 9° | ±0.2° |

**This parameter varies to achieve incidence tolerance (Figure 3)*

The fundamental Reynolds number for profile loss is that based on the suction surface length ($Re_{S_0}$), which characterizes the suction surface boundary layer. This length is not known *a priori* until a profile is designed; in contrast the axial chord is selected much earlier

in the design process. For high aspect ratio blades the endwall loss is largely insensitive to Reynolds number, e.g. [21], therefore for simplicity the calculations are performed at constant $Re_{C_x}$.

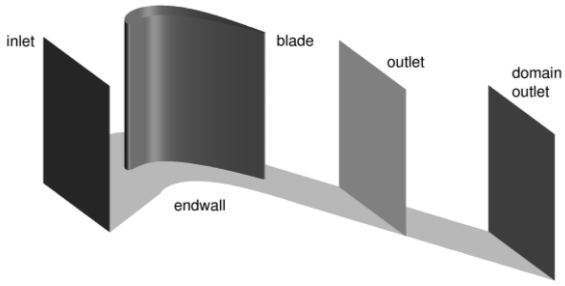


*Figure 4: Typical CFD domain.*

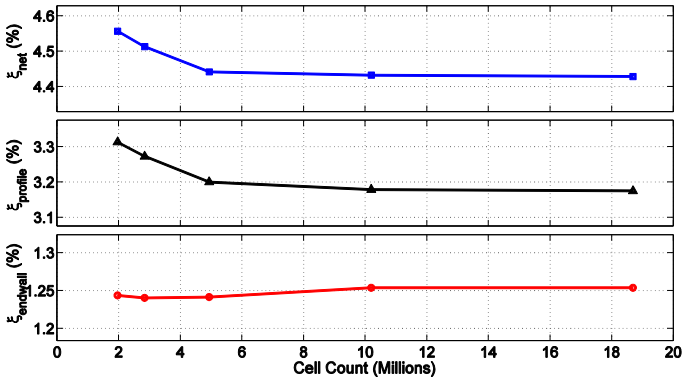


*Figure 5: Mesh sensitivity for a single design ($\alpha_1$=30°, $\alpha_2 = -65°$, $T_{max}/C_x$=0.15).*

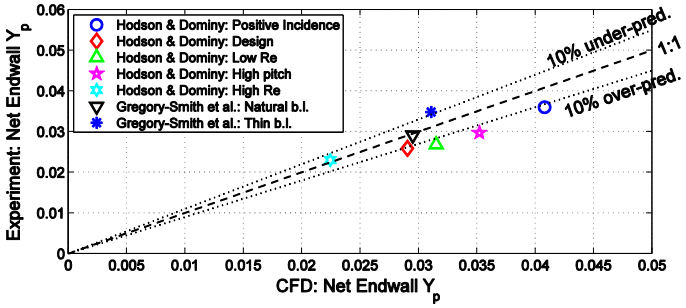


*Figure 6: CFD and experimental endwall losses ([27], [28]).*

## 2.2 Three-Dimensional Meshing and CFD

Automated meshing is performed using an optimizer built around the Rolls-Royce PADRAM code [22], which combines a blade O-mesh with multi-block passage H-meshes. The optimizer drives the input parameters to maximize a mesh quality factor, which incorporates measures of cell skew, aspect ratio, and expansion ratio.

Steady RANS calculations are performed with the Rolls-Royce in-house solver HYDRA; full details of this code are given by Moinier and Giles [23]. The spatial discretization is based on an upwind edge-based finite volume scheme and is second-order accurate.

Calculations are performed using the two-equation SST turbulence model. For simplicity calculations are performed with fully-turbulent boundary layers; while closer agreement with experimental data can be obtained using a transition model ([24]), the fully-turbulent calculations give similar endwall loss predictions and are more robust.

Calculations are performed on a half-passage domain for each linear cascade, with an inviscid wall at midspan to provide symmetry. Figure 4 shows the domain: the inlet is located at a distance of $0.8C_x$ upstream of the leading edge and the domain outlet is $1.2C_x$ downstream of the trailing edge. Spanwise distributions of total pressure, total temperature, flow angles and turbulence parameters are applied at the inlet, and static pressure at the exit. A collinear turbulent boundary layer is specified at the inlet with momentum thickness equal to $0.01C_x$; the distributions are obtained from a separate flat-plate boundary layer calculation. The freestream flow turbulence parameters are set to obtain a turbulence level of 5% with an integral length scale of $0.1C_x$, which is broadly representative of a multistage turbine [25].

The current calculations do not capture the impact of flow unsteadiness on the loss generation, which will introduce some uncertainty in the results. Denton and Pullan [6] examined a linear stage and found that the loss development in the first blade row was approximately equal in steady RANS and unsteady URANS calculations. Therefore the contribution of the unsteadiness to cascade endwall loss is believed to be small; in general this will not be the case in a real turbine where additional unsteadiness is induced by the interaction of adjacent blade rows.

### 2.3 Loss Coefficients

Performance statistics are calculated using the "outlet" plane shown in Figure 4, which is located $0.5C_x$ behind the trailing edge. A constant-area mixing calculation is performed. The entropy loss coefficient ([1]) is defined as the *net* increase between the mixed-out entropy at inlet ($s_{1,mix}$) and exit ($s_{2,mix}$):

$$\xi_{net} = \left(s_{2,mix} - s_{1,mix}\right)\left[T_{2,mix}/\left(h_{02,mix} - h_{2,mix}\right)\right]_{mid} \quad (1)$$

where $h$ is the specific enthalpy. The use of a net loss coefficient aligns with the findings of Sharma and Butler [15], who demonstrated for several cascades that the net mass-averaged loss was approximately independent of the inlet boundary layer thickness. Note that the midspan exit conditions are used as a reference in equation (1), rather than the passage-averaged conditions. This approach has the advantage of ensuring that the profile loss is consistently defined between Mises and RANS calculations.

The total passage loss is split into profile (midspan) and endwall loss using the traditional formulation:

$$\xi_{endwall} = \xi_{net} - \xi_{profile} \quad (2)$$

where $\xi_{profile}$ is calculated from the midspan inlet and exit conditions using equation (1). This breakdown is somewhat arbitrary and can produce strange results, such as negative endwall loss for low aspect ratios (e.g. [26]) or thick inlet boundary layers. The relatively

high aspect ratio ($h/C_x = 3$) and thin inlet boundary layer ($\theta/C_x$=0.01) used in this paper avoid such problems, nonetheless it is recognized that the breakdown of profile and endwall loss is problematic.

### 2.1 Mesh Sensitivity and Validation

Figure 5 shows the calculated loss coefficients as the mesh is refined for a single blade design. The viscous O-mesh and radial distributions are set to maintain a maximum $y^+$ value of approximately unity on the blade and endwall surfaces, with an expansion ratio of 1.14. The final template has 10.2 million cells for this case, and the passage, profile and endwall loss coefficients are within 0.00005 of the finest mesh values.

To assess the accuracy of the CFD set-up, calculations are performed for the Low Pressure turbine cascade of Hodson and Dominy [27] and the High Pressure turbine design studied by Gregory-Smith et al. [28]. Figure 6 compares the measured and predicted endwall losses for different cases; the average error is less than 11%, which is deemed to be acceptable.

## 3 THE TWO-DIMENSIONAL DESIGN SPACE

The designs in Figure 2 represent a family of blades with similar suction side aerodynamics. This section examines the variation within the two-dimensional design space, prior to the discussion of profile (section 4) and endwall losses (section 5).

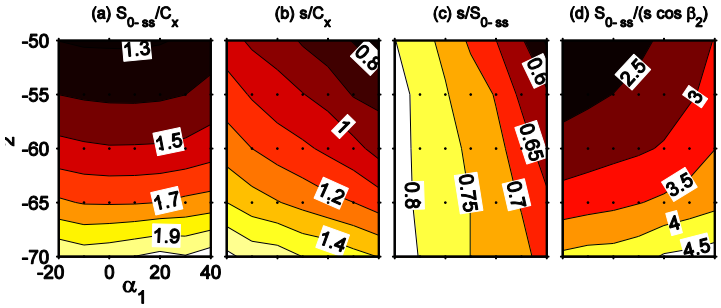


*Figure 7: Geometric Ratios for the designs in Figure 2.*

### 3.1 Surface Length

Figure 7(a) shows the ratio of suction surface length to axial chord ($S_{0-SS}/C_x$), which is largely a function of the exit flow angle, increasing rapidly between $\alpha_2 = -50°$ (~1.3) and $\alpha_2 = -70°$ (~2.0). This length is crucial for the profile loss since it is the characteristic length scale of the suction surface boundary layer, which dominates the loss production. Furthermore since $Re_{C_x}$ is held constant, this ratio sets the characteristic Reynolds number $Re_{S_0}$, which varies between 260,000 ($\alpha_2 = -50°$) and 400,000 ($\alpha_2 = -70°$).

### 3.2 Pitch and Loading Coefficients

The spacing of each blade is determined in the design process by the aerodynamic and thickness targets (see section 2.1), and varies with the flow angles. Figure 7(b) shows the ratio of pitch to axial chord ($s/C_x$) which varies by a factor of around 2, increasing for designs with higher exit angle and lower turning. Figure 7(c) shows the ratio of pitch to suction surface length ($s/S_{0-SS}$), which varies

less strongly and is largely dependent on the inlet flow angle. Circulation arguments show that this ratio is closely related to the turning ([14]).

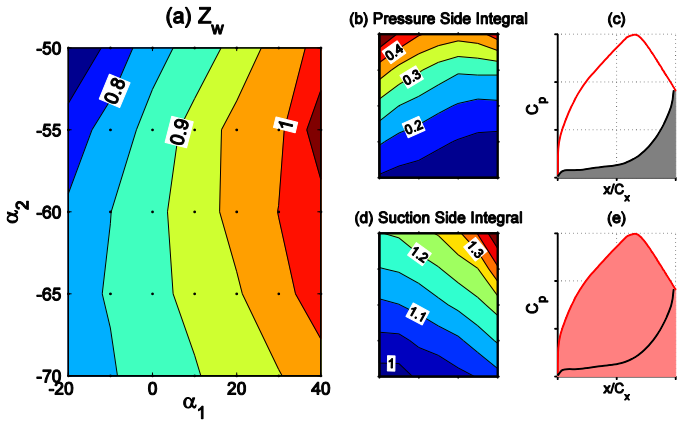


*Figure 8: Zweifel Lift Coefficient ([29]) and breakdown.*

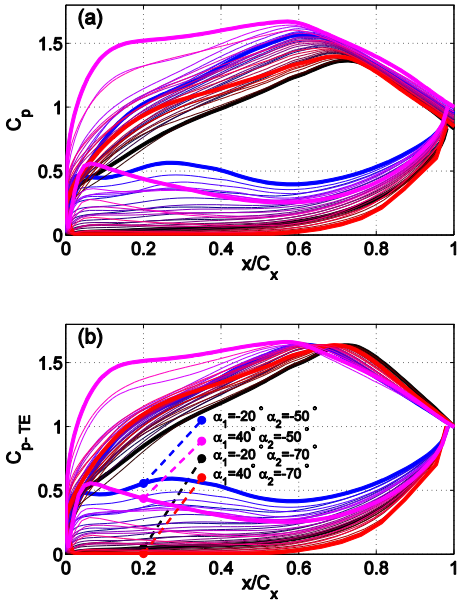


*Figure 9: Mises $C_p$ vs. $x/C_x$ for the designs in Figure 2.*

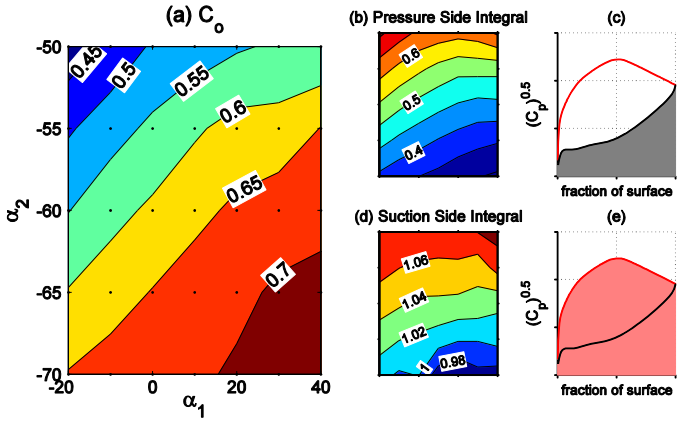


*Figure 10: Circulation Lift Coefficient ([14]) and breakdown.*

The blade pitch may be considered in terms of a lift coefficient. Zweifel [29] calculated the ratio of the blade tangential force to an ideal case ($P_{SS} = P_2$, $P_{PS} = P_{01}$):

$$Z_w = \oint C_p \, d\left(\frac{x}{C_x}\right) = \frac{s}{C_x}\frac{\rho_2 V_2^2 \cos\alpha_2}{(P_{01}-P_2)}\left|\sin\alpha_2 - \frac{V_1}{V_2}\sin\alpha_1\right| \qquad (3)$$

As shown in Figure 8(a), this parameter varies by around 40-45% across the design space, being higher for designs with larger $\alpha_1$. The variation can be understood by splitting the Zweifel coefficient into the negative contribution of the pressure surface integral (Figure 8(b,c)) and the positive contribution of the suction surface integral (Figure 8(d,e)):

$$Z_w = \left[\int_{SS} C_p \, d\left(\frac{x}{C_x}\right)\right] - \left[\int_{PS} C_p \, d\left(\frac{x}{C_x}\right)\right] \qquad (4)$$

The pressure side integral (Figure 8(b)) is higher for low-turning designs, in line with the distributions in Figure 3. Appendix A presents a simple model that demonstrates that this variation is driven by the cross-passage pressure gradient in the covered turning region: in general, the pressure surface velocity will be higher for designs with less deflection and greater thickness. The suction side integral in Figure 8(d) demonstrates a variation of around 40% across the design space, despite the similarity of the suction side $C_p$ distributions in Figure 3. This apparent contradiction arises because the integral in equation (4) is performed with respect to the axial direction; as shown in Figure 9, the distributions of $C_p$ with axial distance vary significantly with flow angles.

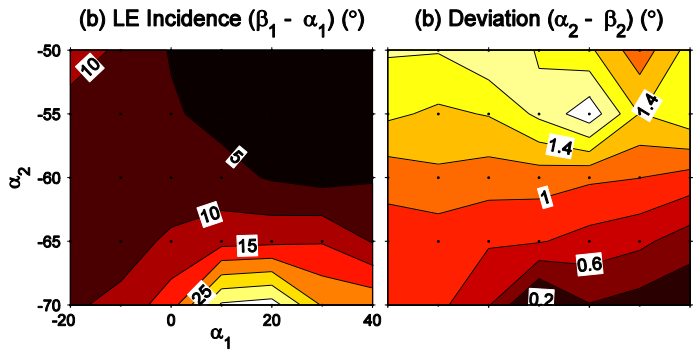


*Figure 11: (a) Leading Edge Incidence (difference between the inlet flow and metal angles) and (b) Deviation (Mises).*

Coull and Hodson [14] argued that the Zweifel coefficient did not adequately account for airfoil camber, and proposed an alternative Circulation Coefficient:

$$C_o = \oint \sqrt{C_p}\, d\left(\frac{S}{S_{0-SS}}\right) \qquad (5)$$

As shown in Figure 10(a), this parameter exhibits a different variation across the design space compared to Zweifel (Figure 8(a)). The Circulation Coefficient can also be decomposed to separate the pressure and suction side contributions:

$$C_o = \left[\int_{SS} \sqrt{C_p} d\left(\frac{S}{S_{0-SS}}\right)\right] - \left(\frac{S_{0-PS}}{S_{0-SS}}\right)\left[\int_{PS} \sqrt{C_p} d\left(\frac{S}{S_{0-PS}}\right)\right] \qquad (6)$$

The ratio of pressure to suction side lengths $S_{0-PS}/S_{0-SS}$ is relatively constant across the design space (0.86 ±0.06). The pressure side integral (Figure 10(b,c)) shows a similar trend to Figure 8(b), but the variation is larger because of the square root in equation (6). As would be expected from the data in Figure 3, the suction side integral is relatively constant, varying by about 10% in line with the local Mach number at the trailing edge (see section 3.4). From this comparison, one may therefore conclude that blade loading coefficient and pitch are determined by the specified suction side $C_p$ design and the pressure side loading, which is predominantly a function of flow angles and thickness (Appendix A).

### 3.3 Incidence and Deviation

As discussed in section 2.1, the design code iteratively droops the leading edge of the blade to prevent over-speed spikes at design and +10° flow incidence. The resultant leading edge incidence, defined as the difference between the inlet flow and metal angles, is presented in Figure 11(a). This parameter is small for much of the design space, but rises significantly for the highest exit angle designs. It should be noted that a manual design of the leading edge shape may produce different results. The deviation relative to the average exit metal angle is presented in Figure 11(b) and remains small across the design space.

### 3.4 Trailing Edge Pressure and Mach number

At the trailing edge plane of a blade row, the freestream velocity tends to be higher than the downstream value because of the combined blockage of the boundary layers and the trailing edge, [1]. However the pressure across this plane is usually non-uniform due to the potential field of the blades, and several authors report high static pressure in the locality of the trailing edge (e.g. [20]). This effect has two competing implications for the blade profile loss. First, for a given peak Mach number the suction surface boundary layer must undergo additional deceleration, increasing the Diffusion Factor, trailing edge momentum thickness [30] and hence the loss. This effect is partly offset by the lower freestream velocity at the boundary layer edge, which implies a lower absolute momentum deficit. Second, higher static pressure around the trailing edge implies higher base pressure on the trailing edge radius, thus the base pressure loss can be reduced and may be negative, e.g. [31], [32].

The variation in trailing edge Mach number is shown in Figure 12(a) for the Mises calculations; the RANS calculations give a very similar result. It can be observed that the Mach number decreases as the exit flow angle increases in magnitude. To a first order this effect is driven by the uncovered turning angle downstream of the blade throat, defined in Figure 13 and plotted in Figure 12(b), which necessitates a pressure gradient normal to the uncovered portion of the suction surface. Figure 12(c) shows the strong correlation between the uncovered turning and the trailing edge Mach number for this set of designs. This relationship is not universal and depends on the blade thickness and suction surface $C_p$ distribution.

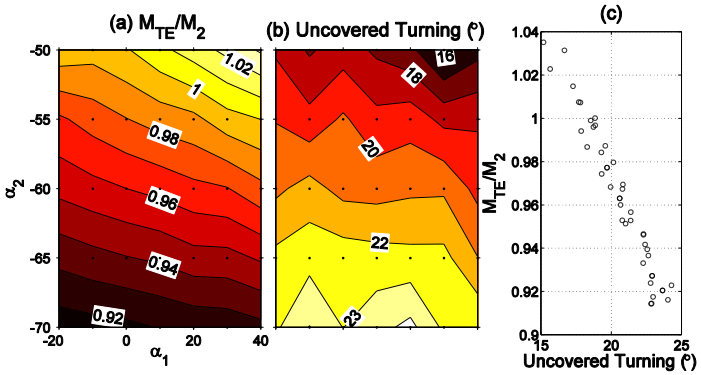


*Figure 12: Trailing Edge Mach number (Mises) and uncovered turning.*

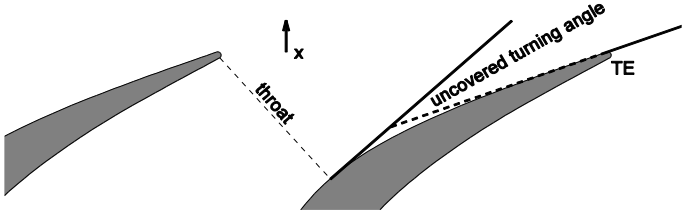


*Figure 13: Definition of uncovered turning angle.*

## 4 PROFILE LOSS

Figure 14(a) and (b) present the mixed-out profile losses calculated using RANS and Mises respectively, both with fully turbulent boundary layers. While there are differences in the level of loss, the trends of the two predictions agree: in general the losses increase for designs with higher turning (bottom right) and higher solidity (top right).

Considering a control volume downstream of a blade throat, Denton [1] derived the following approximation for the mixed-out profile loss:

$$\xi_{Denton} \approx \frac{2(\theta_{SS+PS})}{s\cos\beta_2} + \left(\frac{t + \delta^*_{SS+PS}}{s\cos\beta_2}\right)^2 - \frac{C_{pb}t}{s\cos\beta_2} \qquad (7)$$

where $\theta_{SS+PS}$ and $\delta^*_{SS+PS}$ respectively represent the sum of trailing edge momentum and displacement thickness; $\beta_2$ is the blade metal exit angle; $t$ is the trailing edge thickness and $C_{pb}$ is the base pressure coefficient. The loss coefficient predicted by equation (7) is presented in Figure 14(c) for the Mises results. It shows a similar trend to the calculated losses in Figure 14(b), but there are differences in the overall levels of up to 18%. Michelassi et al. [33] performed Direct Numerical Simulations of unsteady flow around the T106 blade, and noted a discrepancy of around 10-15% between the calculated "steady" loss sources and the terms in equation (7). The current results demonstrate similar differences for steady Mises simulations, indicating that the variance observed by Michelassi is probably due to the assumptions underpinning equation (7), such as zero deviation angle, rather than any unsteady phenomena.

The terms in equation (7) have been extracted from the fully turbulent Mises calculations and are shown in Figure 15. The first term (Figure 15(a)) is the largest and represents the boundary layer momentum deficit. This term is dominated by the suction side contribution which, for a fully-turbulent boundary layer, scales as:

$$\frac{2\,\theta_{SS}}{s\cos\beta_2} = \frac{2\,S_{0-SS}}{s\cos\beta_2} f\left(C_{p-SS}\right) Re_{S_0}^{-0.2} \qquad (8)$$

where $f\left(C_{p-SS}\right)$ will be a constant for designs with matching $C_p$ distributions. The variation in Figure 15(a) is therefore largely driven by the geometric ratio of suction surface length to the effective throat ($S_{0-SS}/s\cos\beta_2$), presented in Figure 7(d). Smaller effects are introduced by the variation in Reynolds number and pressure surface velocity (e.g. Figure 10(b)).

The base pressure loss in Figure 15(c) is the smallest of the three terms and reduces as the trailing edge Mach number drops, becoming negative for high values of uncovered turning (Figure 12). The Mises trailing edge model is approximate but the results are consistent with experimental observations, for example Zhou et al. [32] found a negative base pressure loss for the T106C blade ($\alpha_1 = 32.7°$, $\alpha_2 = -63.7°$).

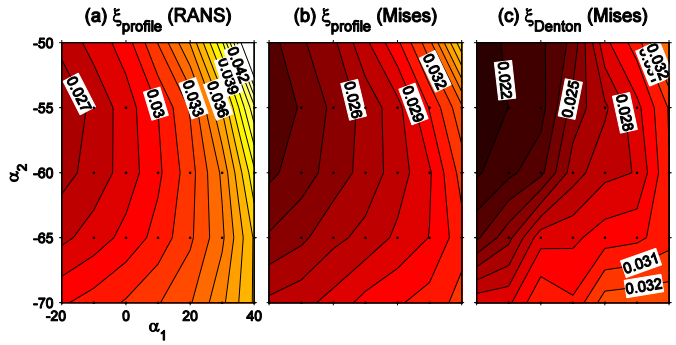


*Figure 14: Fully-turbulent Profile Loss for the designs shown in Figure 2: (a) RANS; (b) Mises; (c) Equation (7) for Mises.*

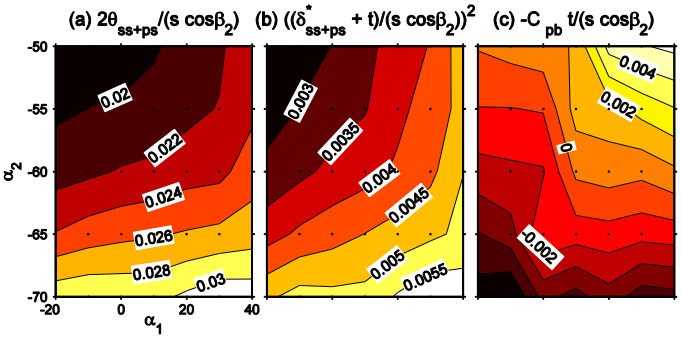


*Figure 15: Breakdown of loss contributions (equation (7)) for fully-turbulent Mises calculations.*

## 5 ENDWALL LOSS

Figure 16 presents the endwall loss coefficients for the designs in Figure 2, which increase for the high-turning designs towards the bottom-right-hand corner of the plot. The level of endwall loss is lower than the profile loss (Figure 14(a)) primarily due to the large aspect ratio of these designs ($h/C_x = 3$). In order to understand the trend in Figure 16, the following analysis approximately separates the endwall loss into contributions from the two primary entropy-generating mechanisms: "background" dissipation in the endwall surface boundary layers; and dissipation induced by the mixing of the secondary flows and their interaction with the surface boundary layers.

### 5.1 "Background" Dissipation Loss

Considering the wetted-area of the endwalls, there is an inevitable entropy generation rate simply due to the presence of boundary layers on these surfaces. This component of loss effectively represents a "background" dissipation rate, i.e. the loss that would occur in the absence of the blade secondary flows (as in the case of a bladeless duct).

Denton [1] described a simple model that assumed constant dissipation coefficient in the boundary layer ($C_D \approx 0.002$). This gives an entropy-generation rate per unit area:

$$d\dot{S}_{surf}/dA = C_D\, \rho_{fs}\, V_{fs}^3/T_{fs} \qquad (9)$$

where $d\dot{S}_{surf}/dA$ is the absolute entropy generation per unit surface area and $V_{fs}$ is the velocity at the edge of the boundary layer. For constant dissipation coefficient, this equation can be integrated to obtain a loss coefficient (after equation (1)):

$$\xi_{CD} \approx 2C_D \left(\frac{A_{endwall}}{h\, s \cos\alpha_2}\right) \int \left(\frac{T_2}{T_{fs}}\right)\left(\frac{\rho_{fs}}{\rho_2}\right)\left(\frac{V_{fs}}{V_2}\right)^3 d\left(\frac{A}{A_{endwall}}\right) \quad (10)$$

This component of loss is therefore inversely proportional to aspect ratio. For the fixed aspect ratio of the current study, Figure 17(a) presents the ratio $A_{endwall}/(h\, s \cos\alpha_2)$, which relates the area of the endwall to the flow cross-sectional area at exit; this factor is predominantly a function of the exit flow angle. The integral in equation (10) depends on the velocity ratio of the cascade (Figure 17(b)) and the velocities inside the blade passage. Two approaches have been taken to estimate this factor:

1. The first method (Figure 17(c)) follows Denton's simple approach and uses information only from the blade pressure distributions. The Mach numbers upstream and downstream of the blade row are taken to be the freestream inlet and exit values respectively. Inside the passage, the freestream Mach number is assumed to vary linearly in the tangential direction between adjacent blade pressure and suction surfaces.
2. In the second approach (Figure 17(d)), the endwall static pressure is extracted from each RANS calculation and used to calculate an isentropic edge Mach number using the inlet freestream conditions.

The two methods give very similar trends, with the former method estimating slightly higher losses. Compared to the overall endwall loss in Figure 16, it can be seen that both models predict a similar level of endwall losses for the low-turning designs in the top-left of the plot. However the overall trend is not captured, and the losses are under-predicted for higher-turning designs which are likely to produce stronger secondary flows (e.g. [34]).

For the remainder of this paper, the background dissipation loss $\xi_{CD}$ in equation (10) is taken from the full integral method (Figure 17(d)) as this is believed to be more accurate. It should, however, be noted that the simple method in Figure 17(c) may be more useful from a preliminary design perspective.

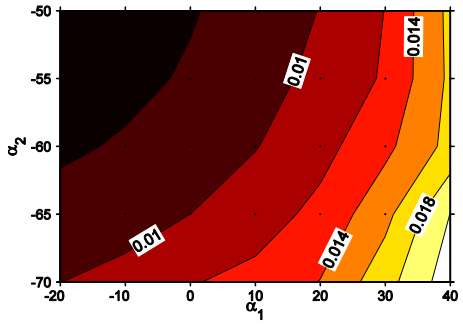


*Figure 16: Endwall Entropy Loss Coefficients.*

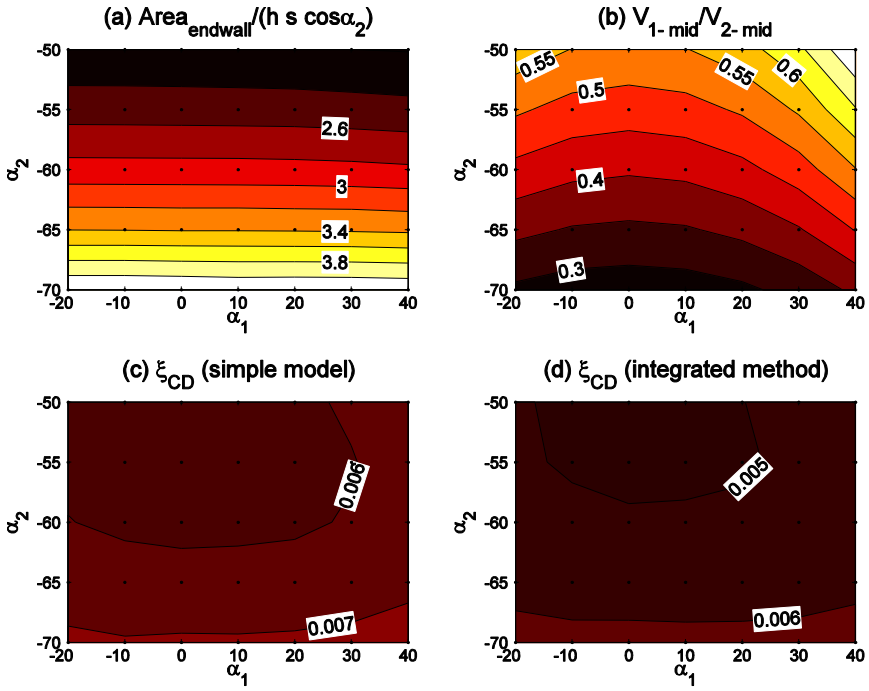


*Figure 17: Models of endwall boundary layer dissipation.*

### 5.2 Secondary-Flow-Induced Loss

Secondary flows induce entropy generation largely through the dissipation of secondary kinetic energy and the mixing-out of low streamwise-momentum fluid. Figure 18(a) presents an estimate of the secondary-flow induced losses, calculated by taking the difference between the endwall loss $\xi_{endwall}$ (Figure 16) and the simple model of endwall boundary layer dissipation loss $\xi_{CD}$ described above (Figure 17(d)):

$$\xi_{sec-flow} = \xi_{endwall} - \xi_{CD} \qquad (11)$$

Figure 18(a) clearly shows the increase in losses for highly-turning designs towards the bottom right of the plot. Squire and Winter [34] produced a simple model of secondary flow in a cascade of turning vanes by considering the convection of inlet boundary layer vorticity through an idealized blade passage with a high axial-chord to pitch ratio. From their equations for the secondary flow components ((21) and (22) in [34]) it can be shown that, for a given inlet profile, the normalized secondary kinetic energy ($ske$) is proportional to:

$$\frac{ske}{0.5\,V_2^2} \propto \left[(\alpha_1 - \alpha_2)\left(\frac{V_1}{V_2}\right)\left(\frac{s\cos\alpha_2}{C_x}\right)\right]^2 \qquad (12)$$

This factor is presented in Figure 18(b). Although it captures the trend of the CFD results to some extent, it does not capture the peak in loss for the highest turning designs in the bottom-right-hand corner of Figure 18(a).

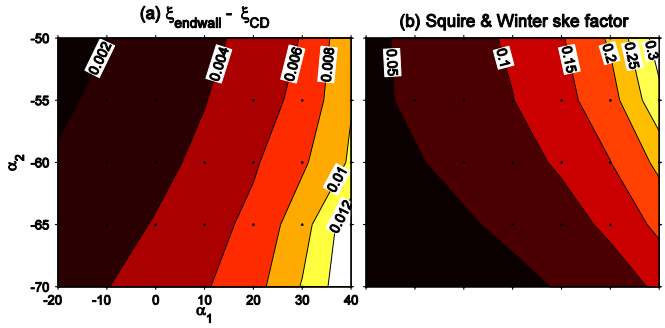


*Figure 18: (a) Estimated contributions from secondary-flow induced loss; (b) the SKE factor of [34] (eq.(12)).*

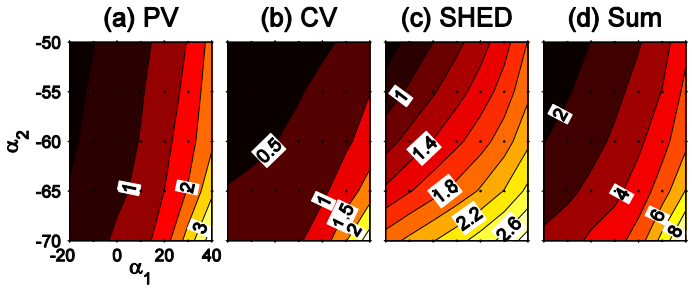


*Figure 19: Vorticity Amplification Factors, after Hawthorne [2].*

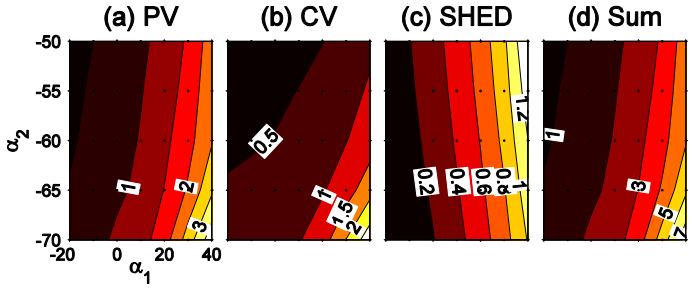


*Figure 20: Vorticity Amplification Factors, after Marsh [35].*

Hawthorne [2] presented a more sophisticated vortex-filament analysis to predict the strengths of the passage and counter vortices (Figure 1) as well as the trailing edge shed vorticity. The method predicts the orientation of the downstream vortex filament by considering the difference in transit times of flow passing over the pressure and suction surfaces. Non-dimensionally, this time difference may be written as:

$$\Delta T^* = T^*_{PS} - T^*_{SS} = \int_{PS} \left(\frac{V_2}{V_{fs}}\right) d\left(\frac{S}{C_x}\right) - \int_{SS} \left(\frac{V_2}{V_{fs}}\right) d\left(\frac{S}{C_x}\right) \quad (13)$$

where $V_{fs}$ is the freestream velocity at the edge of the boundary layer. The Hawthorne analysis predicts stronger secondary flows when the pressure surface velocity is low, and is therefore sensitive to the significant variation in pressure side velocities around the design space (Figure 3, Figure 10(b)). This sensitivity can also be understood with reference to the basic flow physics: since low velocity fluid

on the pressure surface lacks streamwise momentum, it is more susceptible to the cross-passage pressure gradients and thus the secondary flow will be stronger.

Hawthorne derived relationships for the streamwise circulation of the distributed passage vortex (PV), counter vortex (CV) and trailing edge shed vortex (SHED). These equations are here presented as non-dimensional vorticity amplification factors, which represent the ratio of outlet streamwise vorticity to the inlet boundary layer vorticity:

$$AF = \frac{\Gamma_{sec} / \left(\frac{V_2}{C_x}\frac{h}{2} s \cos\alpha_2\right)}{\overline{\omega_1}/(V_1/C_x)} \qquad (14)$$

where $\Gamma_{sec}$ is the secondary circulation at the cascade outlet, which is normalized using the exit velocity and flow area of the half-passage cascade. For the constant aspect ratio and boundary layer height employed in this study, the inlet vorticity $\overline{\omega_1}$ is simply proportional to the inlet velocity $V_1$.

Hawthorne's amplification factors may be expressed as (after equations (26), (32) and (37) in [2]):

$$AF_{PV} = \left(\frac{V_1}{V_2}\right)^2 \left( \frac{\Delta T^* C_x}{s\cos\alpha_2} + \frac{\left|\frac{V_2}{V_1}\sin\alpha_1 - \sin\alpha_2\right|}{\cos\alpha_2} \right) \qquad (15)$$

$$AF_{CV} = -\left(\frac{V_1}{V_2}\right)^2 \frac{\Delta T^* C_x}{s\cos\alpha_2} \qquad (16)$$

$$AF_{SHED} = -\left(\frac{V_1}{V_2}\right)\frac{\cos\alpha_1}{\cos\alpha_2}\left|\tan\alpha_2 - \tan\alpha_1\right| \qquad (17)$$

The magnitude of these three factors are plotted in Figure 19, together with the summation. Immediately it can be seen that the passage vortex factor and the summation approximately follow a similar trend to the estimated secondary-flow-induced loss in Figure 18(a), reinforcing the assertion that these losses are driven by the secondary flows.

Using a different approach, Marsh [35] applied Kelvin's circulation theory and included the effect of compressibility. The amplification factors are calculated by integrating Marsh's expressions for vorticity (equations (42), (51) and (63) in [35]) across the exit flow area to obtain the total circulation:

$$AF_{PV} = M^* \left(\frac{V_1}{V_2}\right)^2 \left[ \frac{\Delta T^* C_x}{s\cos\alpha_2} + \frac{\left|\frac{V_2}{V_1}\sin\alpha_1 - \sin\alpha_2\right|}{\cos\alpha_2} \right] \qquad (18)$$

$$AF_{CV} = -\left(\frac{V_1}{V_2}\right)\left( M^* \frac{V_1}{V_2}\frac{\Delta T^* C_x}{s\cos\alpha_2} + \frac{(M^*-1)}{\cos\alpha_2}\left|\frac{V_2}{V_1}\sin\alpha_2 - \sin\alpha_2\right| \right) \qquad (19)$$

$$AF_{SHED} = -\left(\frac{V_1}{V_2}\right)\left(\frac{M^*}{\cos\alpha_2}\left|\frac{V_1}{V_2}\sin\alpha_2 - \sin\alpha_1\right| - \frac{(M^*-1)}{\cos\alpha_2}\left|\frac{V_2}{V_1}\sin\alpha_2 - \sin\alpha_1\right|\right) \quad (20)$$

where the compressibility factor $M^*$ is given by:

$$M^* = \left(1 + \frac{\gamma - 1}{2}M_1^2\right) \quad (21)$$

For the current designs this factor varies between about 1 and 1.04, indicating relatively modest compressibility effects in line with the findings of Marsh [35].

Figure 20 shows the magnitude of Marsh's amplification factors (equations (18)→(20)) and their summation. As inspection of the above equations shows, the distributions of the passage and counter vortex factors are almost identical to those of Hawthorne. However the shed vorticity factor is markedly different, as discussed by Came and Marsh [36]. The overall summation in Figure 20(d) has the same trend as the estimated secondary-flow-induced loss in Figure 18(a).

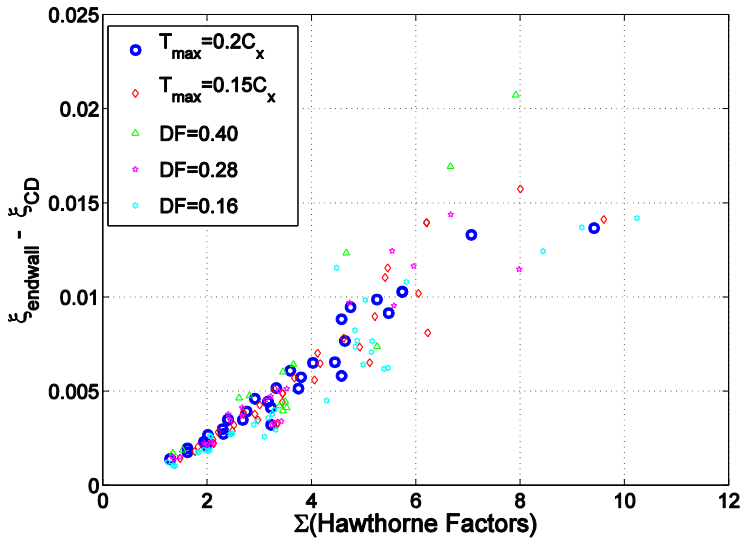


*Figure 21: Comparison of Estimated Secondary-Flow-Induced loss and the summed Amplification Factor of Hawthorne [2].*

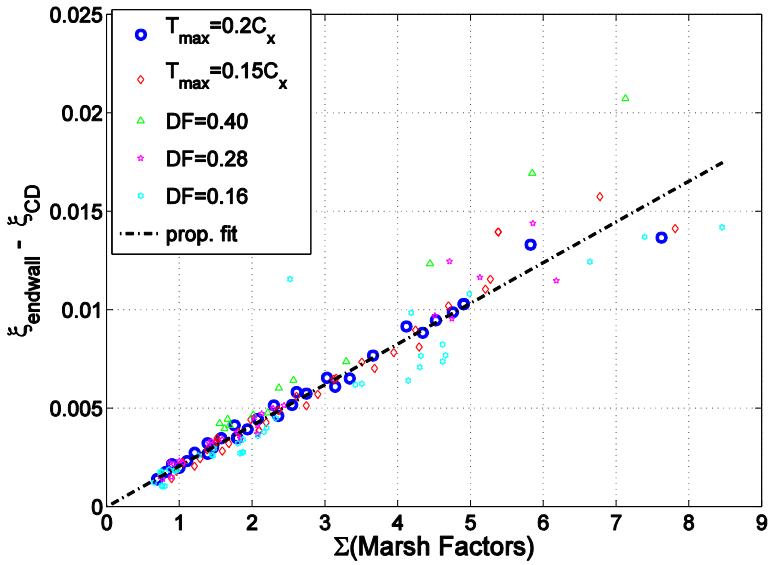


*Figure 22: Comparison of Estimated Secondary-Flow-Induced loss and the summed Amplification Factor of Marsh [35].*

Figure 21 and Figure 22 present quantitative comparisons of the estimated secondary-flow-induced loss and the summed amplification factors of Hawthorne and Marsh. The designs from Figure 2 are labeled ($T_{max} = 0.2C_x$), and around 120 additional blade designs have been included in these plots. These include a set of 35 designs matching those in Figure 2, but with lower maximum thickness ($T_{max} = 0.15C_x$) and trailing edge wedge angle (6°). The surface $C_p$ distributions for these thinner designs are shown in Figure 23, and are very similar to those presented in Figure 3. The reduction in the passage blockage causes two main differences with the thicker set: there is a less pronounced overspeed on the early suction surface for the $\alpha_1 = 40°$, $\alpha_2 = -50°$ design; and the pressure-side velocities are slightly lower, an effect captured by the simple model in Appendix A. Also included in Figure 21 and Figure 22 is a survey of different $C_p$ design styles with the original thickness distribution, conducted by varying Diffusion Factor (0.16, 0.28, 0.40) and Peak Suction Location (0.42, 0.52, 0.62). These designs approximately correspond to the parametric set of high-lift low pressure turbine designs studied by Coull et al. [18], and are labeled by the Diffusion Factor (DF) in Figure 21 and Figure 22.

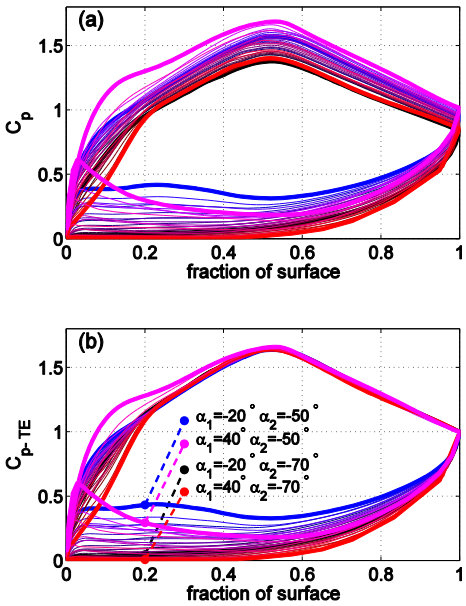


*Figure 23: Mises $C_p$ distributions for the thinner designs.*

While there is a definite trend with the Hawthorne analysis in Figure 21, the near-proportional correlation with the Marsh amplification factor in Figure 22 is compelling. The secondary-flow-induced-loss approximately collapses onto the trend:

$$\xi_{MARSH-fit} \approx 0.0021\, AF_{Marsh} \qquad (22)$$

where the summed Amplification Factor $AF_{Marsh}$ is given by:

$$AF_{Marsh} = 2M^* \left(\frac{V_1}{V_2}\right)^2 \left[\frac{\Delta T^* C_x}{s \cos \alpha_2} + \frac{\left|\frac{V_2}{V_1} \sin \alpha_1 - \sin \alpha_2\right|}{\cos \alpha_2}\right] \qquad (23)$$

There is some scatter from this best fit line, of the order of ±0.0015 for most designs but rising significantly for the designs with the highest secondary-flow-induced losses (>0.008).

It should be noted that despite its satisfying simplicity and accuracy, the fit in equation (22) is empirical and further work is needed to understand its physical basis. The increase in scatter for designs with large secondary flows also needs to be understood. Preliminary investigations suggest that some of this scatter is an artifact of the finite aspect ratio used in the study ($h/C_x$ = 3). Even at this relatively large aspect ratio, strong secondary flows will induce some streamtube contraction at midspan and hence affect the breakdown of profile and endwall loss in equation (2). Marsh's theory may also be less applicable to these designs, particularly since it does not account for the significant stream surface twist. Finally it is noted that in this study the inlet boundary layer thickness has been scaled with the blade axial chord, which is likely to be somewhat arbitrary when considering the impact of inlet conditions on secondary flow. It will remain for future investigations to examine these effects.

### 5.3 Overall Endwall Loss: A Simple Method

From the above analysis, cascade endwall loss can be estimated by the summation of two components:

1. **"Background" Dissipation Loss $\xi_{CD}$** (equation (10)) based on a constant dissipation coefficient ($C_D = 0.002$) and an estimate of the freestream velocity above the endwall boundary layers (described in section 5.1, Figure 17(d)).
2. **Secondary-Flow-Induced Loss $\xi_{MARSH-fit}$** (equation (22)), which is approximately proportional to the vorticity amplification factor after Marsh [35] (equation (22), Figure 22).

Figure 24 compares the result of this method with the calculated endwall losses for all of the designs studied (around 150 in total). The average discrepancy is 5.0%, with most of the cases falling within ±10% of the correlated values.

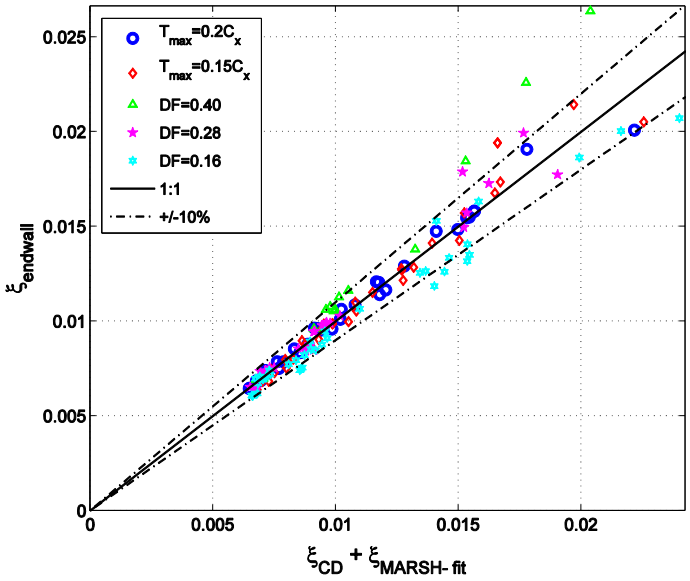


*Figure 24: Endwall Loss: Simple Model vs. CFD.*

The method can be generalized for cascades with different aspect ratio: the endwall boundary layer dissipation in equation (10) already has the correct sensitivity, while the secondary-flow-induced loss should be scaled with the inverse of aspect ratio. The method is only strictly valid for the inlet condition studied (collinear turbulent boundary layer with $\theta/C_x$=0.01), and further work is needed to extend the approach to different inlet conditions.

## 6 CONCLUSIONS

A parametric design study has been conducted to examine the impact of key design variables on endwall loss in turbine cascades. The impact of flow angles, blade thickness and suction surface aerodynamics have been studied and the following conclusions are drawn:

- The pressure side velocity is largely determined by the cross-passage pressure gradient in the covered turning region, being lower for higher-turning and thinner designs. The variation affects both the blade lift coefficient and the endwall losses.

- The Zweifel lift coefficient is highly dependent on flow angles and is not a universal measure of blade loading. For designs with matching suction surface $C_p$ distributions, the *suction surface contribution* to Zweifel varies by up to 40% as the flow angles change. A lift coefficient based on circulation ([14]) allows a more consistent comparison across the design space.
- Endwall loss may be separated into the contributions of: (1) dissipation in the endwall boundary layers, and (2) losses induced by the secondary flow, which includes the dissipation of secondary kinetic energy.
- Secondary-flow-induced loss scales almost linearly with a vorticity amplification factor derived using the method of Marsh [35].
- A simple model is presented which captures the calculated endwall loss for designs with different flow angles, thickness distributions and suction surface $C_p$ distributions. The average discrepancy between modeled and calculated endwall loss is around 5%, with higher scatter for designs with stronger secondary flow.
- The model developed is based on physical principles with a single correlation coefficient. The method achieves good accuracy for the cases studied, which span a significant proportion of the design space, and thus provides a suitable basis for a low-order prediction of cascade endwall loss.

Further work is needed to examine the effects of inlet conditions and aspect ratio, and to relate cascade endwall loss to real turbine behavior.

## ACKNOWLEDGMENTS

The author would like to acknowledge the funding, support and permission to publish from Rolls-Royce plc; in particular to Frederic Goenaga, Raul Vazquez, and Giulio Zamboni. The author also thanks Howard Hodson, John Denton, Graham Pullan, Chris Clark and Shaun Kaufmann of the Whittle Laboratory for their input.

## NOMENCLATURE

**Symbols**

$A$ Area

$AF$ Vorticity Amplification Factor (equation (14))

$AR$ Aspect Ratio $= h/C_x$

$C_D$ Dissipation Coefficient

$C_o$ Circulation Coefficient $= \oint \sqrt{C_p}\, d(S/S_{0-SS})$, [14]

$C_p$ Pressure Coefficient $= (P_{01} - P)/(P_{01} - P_2)$

$C_{p-TE}$ $C_p$ Referenced to TE $= (P_{01} - P)/(P_{01} - P_{TE})$

$C_{pb}$ Base Pressure Coefficient $= (P_{base} - P_2)/(P_{01} - P_2)$

$C_x$ Axial Chord

$DF$ Diffusion Factor $= \sqrt{(C_{p-TE}(peak) - 1)}$

$h$ Span, or Specific Enthalpy (equation (1) only)

$M$ Mach number

$P$, $P_0$ Static and Total Pressure

$PSL$ Peak Suction Location $= s_{SS}(peak)/s_{0-SS}$

$Re_{c_x}$ Axial Chord Reynolds number $= V_2 C_x/\upsilon$

$Re_{s_0}$ Suction Surface Reynolds number $= V_2 S_{0-SS}/\upsilon$

$s$ Pitch (Spacing), or Specific Entropy (equation (1) only)

$S$ Distance along Surface

$S_0$ Total Surface Length

$t$ Trailing Edge Thickness

$T$ Temperature

$T^*$ Non-Dimensional Surface Transit Time

$T_{max}$ Maximum Blade Thickness

$V$ Velocity

$x$ Axial Distance

$Y_p$ Total Pressure Loss Coefficient

$Z_w$ Zweifel Lift Coefficient

$\alpha$ Flow Angle

$\beta$ Metal Angle

$\Gamma$ Circulation

$\rho$ Density

$\upsilon$ Kinematic Viscosity

$\xi$ Entropy Loss Coefficient (see equation (1))

$\overline{\omega_1}$ Mass-Averaged Inlet Boundary Layer Vorticity

**Subscripts and Abbreviations**

0 Stagnation

1, 2 Row Inlet and Outlet

$CD$ Endwall Boundary Layer Dissipation

$fs$ Boundary layer edge

$LE$ Leading Edge

$mid$ Midspan

$mix$ Mixed-Out (Constant-Area)

$peak$ Peak Suction Location on Suction Surface

$PS$ Pressure Surface

S$S$ Suction Surface

$TE$ Trailing Edge

## REFERENCES


[1] Denton, JD, 1993, "Loss Mechanisms in Turbomachines" ASME. *J. Turbomach., Vol. 115(4), pp. 621-656*

[2] Hawthorne, WR, 1955, "Rotational Flow Through Cascades: Part 1: The Components of Vorticity", *Quart. Journ. Mech. and Applied Math.*, Vol 8(3)

[3] Sieverding, CH, 1985, "Recent Progress in the Understanding of Basic Aspects of Secondary Flows in Turbine Blade Passages", ASME. *J. Eng. Gas Turbines Power.* 1985;107(2) pp. 248-257

[4] Langston, LS, 2001, "Secondary flows in axial turbines—a review" *Annals of the New York Academy of Sciences* 934.1 (2001) pp. 11-26

[5] Adrian, RJ, Christensen, KT, and Liu, Z-C, 2000, "Analysis and interpretation of instantaneous turbulent velocity fields" *Experiments in Fluids*, Vol. 29, pp. 275-290

[6] Denton, JD and Pullan, GP, 2012, "A Numerical Investigation into the Sources of Endwall Loss in Axial Flow Turbines", ASME paper GT2012-69173

[7] Pullan, GP, Denton, JD, and Dunkley, M, 2003 "An Experimental and Computational Study of the Formation of a Streamwise Shed Vortex in a Turbine Stage." ASME. *J. Turbomach.*, 125(2), pp. 291-297.

[8] Ainley, DG and Mathieson, GCR, 1957, “A Method of Performance Estimation for Axial-Flow Turbines”, *ARC Reports and Memoranda* No. 2974

[9] Dunham, J, and Came, PM, 1970, “Improvements to the Ainley-Mathieson method of turbine performance prediction”, ASME, *Jnl. Eng. Power*, July 1970

[10] Kacker, SC and Okapuu, U, 1982, “A Mean Line Performance Method for Axial Flow Turbine Efficiency”, *Journal of Engineering for Power* Vol. 104 pp.111-119

[11] Craig, HRM, and Cox, HJA, 1971, “Performance estimation of axial flow turbines”, *Proc. I. Mech. E.,* Vol. 185 32/71, 1970-71

[12] Traupel, W, 1977, “Thermische Turbomaschinen” Springer-Verlag

[13] Benner, MW, Sjolander, SA, and Moustapha, SH, 2006, “An Empirical Prediction Method For Secondary Losses In Turbines – Part II: A New Secondary Loss Correlation”, ASME. *J. Turbomach.,* Vol. 128(2), pp. 281-291

[14] Coull, JD, and Hodson, HP, 2013, "Blade Loading and Its Application in the Mean-Line Design of Low Pressure Turbines." *Journal of Turbomachinery* 135(2), 021032.

[15] Sharma OP, and Butler, TL, 1986, "Predictions of Endwall Losses and Secondary Flows in Axial Flow Turbine Cascades." ASME Paper 86-GT-228, International Gas Turbine Conference and Exhibit, Dusseldorf, West Germany, June 8–12

[16] Drela, M, 1985, “Two-Dimensional Transonic Aerodynamic Design and Analysis Using the Euler Equations”, PhD Thesis, Massachusetts Institute of Technology

[17] Youngren, H, and Drela, M, 1991 "Viscous/inviscid method for preliminary design of transonic cascades." *AIAA Paper* 91-2364

[18] Coull, JD, Thomas, RL and Hodson, HP, 2010, “Velocity Distributions for Low Pressure Turbines”, ASME. *J. Turbomach.,* Vol. 132(4), 041006

[19] Goodhand, MN, & Miller, RJ, 2011. “Compressor Leading Edge Spikes: A New Performance Criterion”, ASME. *J. Turbomach., 133*(2), 021006

[20] Howell, RJ, Ramesh, ON, Hodson, HP, Harvey, NW, Schulte, V, 2001, “High Lift and Aft-Loaded Pressure Profiles for Low-Pressure Turbines” ASME. *J. Turbomach.,* Vol. 123(2), pp. 181-188

[21] Vázquez, R, Torre, D, Partida, F, Armañanzas, L, and Antoranz, A, 2011, "Influence of Surface Roughness on the Profile and End-Wall Losses in Low Pressure Turbines” ASME Turbo Expo Paper GT2011-46371, Dusseldorf, West Germany, June 8–12

[22] Shahpar, S, and Lapworth, L, 2003, “PADRAM: Parametric Design and Rapid Meshing System for Turbomachinery Optimisation”, ASME Turbo Expo, Paper GT2003-38698, June 16–19, 2003, Atlanta, Georgia, USA

[23] Moinier, P, and Giles, MB, 1998, "Preconditioned Euler and Navier-Stokes Calculations on Unstructured Grids", 6th ICFD Conference on Numerical Methods for Fluid Dynamics

[24] Menter, FR, Langtry, RB, Likki, SR, Suzen, YB, Huang, PG and Völker, S, 2006, “A Correlation-Based Transition Model Using Local Variables—Part I: Model Formulation” ASME. *J. Turbomach.,* Vol. 128(3), pp. 413-422

[25] Halstead, DE, 1996, “Boundary Layer Development in Multi-Stage Low Pressure Turbines” PhD Thesis, Iowa State University

[26] Benner, MW, Sjolander, SA and Moustapha, SH, 2006, "An Empirical Prediction Method for Secondary Losses in Turbines - Part I: A New Loss Breakdown Scheme and Penetration Depth Correlation." ASME. *J. Turbomach.,* Vol. 128(2), pp. 273-280

[27] Hodson, HP and Dominy, RG, 1987, “The Off-Design Performance of a Low-Pressure Turbine Cascade” ASME. *J. Turbomach.,* Vol. 109(2), pp. 201-209

[28] Gregory-Smith, DG, Graves, CP, and Walsh, JA, 1988, “Growth of Secondary Losses and Vorticity in an Axial Turbine Cascade”, ASME. *J. Turbomach.,* Vol. 110(1), pp. 1-8

[29] Zweifel, O, 1945, “The Spacing of Turbomachine Blading, Especially with Large Angular Deflection” Brown Boveri Rev. 32-12

[30] Coull, JD, & Hodson, HP, 2012, “Predicting the Profile Loss of High-Lift Low Pressure Turbines” ASME. *J. Turbomach.,* Vol. 134(2), 021002

[31] Curtis, EM, Hodson, HP, Banieghbal, MR, Denton, JD, Howell, RJ, and Harvey, NW, 1997, “Development of blade profiles for low-pressure turbine applications” ASME. *J. Turbomach.,* Vol. 119(3), pp. 531-538

[32] Zhou, C, Hodson, HP, and Himmel, C, 2014, "The Effects of Trailing Edge Thickness on the Losses of Ultra-High Lift LP Turbine Blades" ASME. *J. Turbomach.,* Vol. 136(8), 081011

[33] Michelassi, V, Chen, LW, Pichler, R, & Sandberg, RD, 2015, “Compressible Direct Numerical Simulation of Low-Pressure Turbines—Part II: Effect of Inflow Disturbances” ASME. *J. Turbomach.,* Vol. 137(7), 071005

[34] Squire, HB and Winter, KG, 1951, “The Secondary Flow in a Cascade of Airfoils in a Nonuniform Stream”, *Journal of the Aeronautical Sciences,* April 1951

[35] Marsh, H, 1976, “Secondary Flow in Cascades – The Effect of Compressibility”, *Aeronautical Research Council R&M* No. 3778

[36] Came, PM and Marsh, H, 1974, “Secondary Flow in Cascades: Two Simple Derivations for the Components of Vorticity”, *Journal Mechanical Engineering Science,* Vol. 16(6), pp. 391-401

[37] Hodson, HP, 2012, “Blade To Blade Flowfields in Axial Turbomachines”, Cambridge Turbomachinery Course 2012, Vol. 1, pp. 35-75

## APPENDIX A: PRESSURE-SIDE LOADING MODEL

In order to understand the trends observed in pressure side loading (Figure 8(b) and Figure 10(b)), Figure 25 presents a simple model for the covered turning region (after Hodson [37]). The flow is assumed to rotate as a free vortex between two circular arcs which approximate the suction and pressure sides of adjacent blades. From the geometry shown, the radii of curvature are:

$$R_{PS} = C_x/(\sin\alpha_1 - \sin\alpha_2) \quad \text{(A1)}$$

$$R_{SS} = C_x/(\sin\alpha_1 - \sin\alpha_2) - (s - T_{max}) \quad \text{(A2)}$$

A limit of $R_{SS} \geq 0$ is applied to prevent non-physical solutions in some cases. For simplicity the flow is taken as incompressible. Considering the pressure gradient across the passage (Figure 25(b)), one can obtain:

$$\frac{dP}{dy} = \frac{\rho V^2}{R} \approx \frac{2}{R(y)}(P_0 - P(y)) \quad \text{(A3)}$$

$$\Rightarrow \frac{P_0 - P(y)}{P_0 - P_{PS}} = \left(\frac{V(y)}{V_{PS}}\right)^2 = \left(\frac{R_{PS}}{R_{SS} + y}\right)^2 \quad \text{(A4)}$$

Integrating across the passage, the mass flow per unit span can be equated to the value at exit. Using the result in equation (A4):

$$\rho V_2 s \cos\alpha_2 = \int_0^{s-T_{max}} \rho V_{PS}\left(\frac{R_{PS}}{R_{SS} + y}\right) dy \quad \text{(A5)}$$

$$\Rightarrow \frac{V_{PS}}{V_2} = \sqrt{C_{p-PS}} = \left(\frac{s\cos\alpha_2}{R_{PS}}\right) / \ln\left(\frac{R_{PS}}{R_{SS}}\right) \quad \text{(A6)}$$

Predictions of $\sqrt{C_{p-PS}}$ using this equation are shown in Figure 26 for a range of flow angles and two different thickness distributions. Figure 26(a) shows predictions for the set with maximum thickness $T_{max} = 0.15C_x$, discussed in section 5.2. Figure 26(b) shows the results for the thicker designs in Figure 2. In general, the pressure surface velocity increases for designs with low deflection and larger thickness. The predictions can be compared with the pressure-side integral of the Circulation Coefficient (equation (6)) for the two sets of design, presented in Figure 27. It can be seen that the overall trend with flow angles and thickness is captured, but the free vortex model predicts a lower value since it does not capture the rapid pressure surface acceleration towards the trailing edge (e.g. Figure 3).

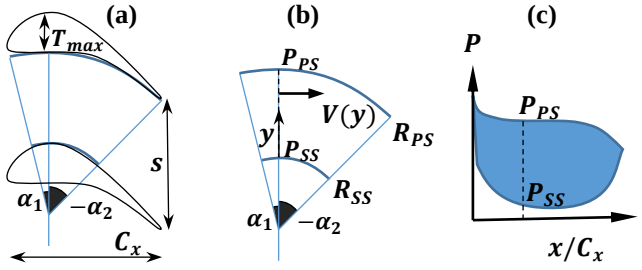


*Figure 25: Free-vortex model for the covered turning region.*

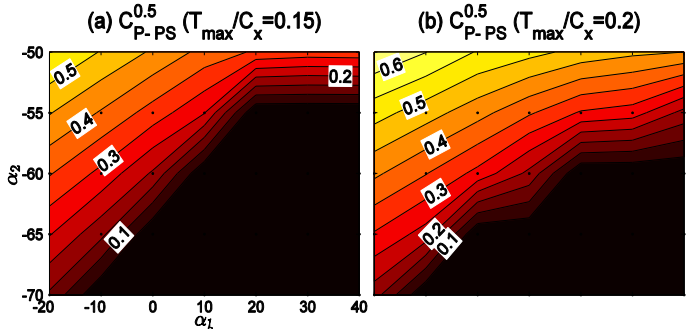


*Figure 26: Free-Vortex model of $\sqrt{C_{P-PS}}$ for the thin (a) and thick (b) sets of blades.*

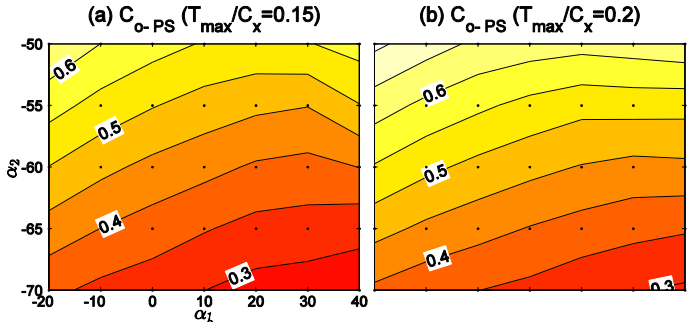


*Figure 27: Pressure-side Circulation integral for the thin (a) and thick (b) sets of blades, from Mises design calculations.*